

# What can we learn from the experiment of electrostatic conveyor belt for excitons?

T. T. Zhao,<sup>1</sup> Rui Li,<sup>1</sup> and C. S. Liu<sup>1,\*</sup>

<sup>1</sup>*Key Laboratory for Microstructural Material Physics of Hebei Province,  
School of Science, Yanshan University, Qinhuangdao 066004, China*

(Dated: June 19, 2024)

Motivated by the experiment of electrostatic conveyor belt for indirect excitons [A. G. Winbow, *et al.*, Phys. Rev. Lett. **106**, 196806 (2011)], we study the exciton patterns for understanding the exciton dynamics. By analyzing the exciton diffusion, we find that the patterns mainly come from the photoluminescence of two kinds of excitons. The patterns near the laser spot come from the hot excitons which can be regarded as the classical particles. However, the patterns far from the laser spot come from the cooled excitons or coherent excitons. Taking into account of the finite lifetime of Bosonic excitons and of the interactions between them, we build a time-dependent nonlinear Schrödinger equation including the non-Hermitian dissipation to describe the coherent exciton dynamics. The real-time and imaginary-time evolutions are used alternately to solve the Schrödinger equation in order to simulate the exciton diffusion accompanied with the exciton cooling in the moving lattices. By calculating the escape probability, we obtain the transport distances of the coherent excitons in the conveyor which are consistent with the experimental data. The cooling speed of excitons is found to be important in the coherent exciton transport. Moreover, the plateau in the average transport distance cannot be explained by the dynamical localization-delocalization transition induced by the disorders.

## I. INTRODUCTION

A particle is usually called as a quantum walkers when its time evolution follows the rules of quantum mechanics. Standard quantum mechanics assumes Hermiticity of the Hamiltonian. However, non-Hermiticity is a universal phenomenon in many fields of physics, such as the dissipative systems with gain and loss [1]. As a result, the non-Hermitian quantum walker is of universal significance and has attracted attention recently [2–5]. The direct observation of a quantum walker is very difficult whether it is in Hermitian or in non-Hermitian systems. Taking the particle in a one-dimensional periodic potential as an example, if the potential is in time, the number of the particle transport for the simplest quantum walker during the time cycle equals to the Chern number. The Chern number characterizes the topological structure of the model mapping from the parameter space of wave vector and time ( $k, t$ ) to the momentum space ( $k_x, k_y$ ) [6]. The gedanken experiment considered by Thouless demands adiabatic approximation, i.e. very slowly changing potential. In particular, the particles must be the Fermions occupying in a filled Bloch bands at zero temperature.

The excitons, Bosonic quasiparticles, are the electron-hole bound pairs in semiconductor which are expected to realize Bose-Einstein condensation [7]. Due to the finite lifetime, the exciton systems have the endogenously non-Hermiticity. Both the short lifetime and the low cooling rate hinder the realizing of the Bose-Einstein condensation. In order to overcome the above two disadvantages, the indirect excitons, i.e. the spatially sepa-

rated electron-hole bound pairs, were generated in coupled quantum wells [8]. As their neutral overall, they are harder to manipulate electrically. However, the energy of the indirect excitons can be controlled by voltage due to the dipole moment. By applying an alternating voltage to an electrode grid that covers the device, a wavelike potential was created for the excitons. The excitons are modulated by the wavelike potential which acts as the conveyor belt across the sample. Since the high density of excitons has the high luminous intensity, the exciton pattern allows us to track the location of the excitons. The exciton pattern in the moving lattices, or the conveyor belt, gives the opportunity to observe the non-Hermitian quantum walker.

The data of electrostatic conveyor belt for indirect excitons were reported in Ref. [9]. [(a) and (b)], [(c) and (d)] and [(e) and (f)] in Fig. 1 show the  $x$ - $y$  photoluminescence (PL) images,  $x$ -energy PL images and  $x$ -PL intensity respectively for conveyor off and on. The left column of the last row [Fig. 1 (g)] shows the average transport distance of indirect excitons via conveyor  $M_1$  as a function of the conveyor amplitude. Fig. 1 (h) shows the distance of indirect excitons via the conveyor  $M_1$  as a function of density. The first moment of the PL intensity  $M_1 = \int xI(x)dx / \int I(x)dx$ , which characterizes the average transport distance of the indirect excitons via conveyor.  $I(x)$  is the PL intensity profile obtained by the integration of the  $x$ -energy images over the emission wavelength. Major features of the indirect exciton transport are summarized as follow. (i) There exist the dynamical localization-delocalization transitions. (ii) Crossing the transition point, the transport distance increases with the conveyor amplitude and tends to saturation. (iii) The exciton transport is less efficient for higher velocity. (iv) The efficient exciton transport via the conveyor only occurs at intermediate densities. (v)

\* cslu@ysu.edu.cn

Several bright stripes are shown in the PL images.

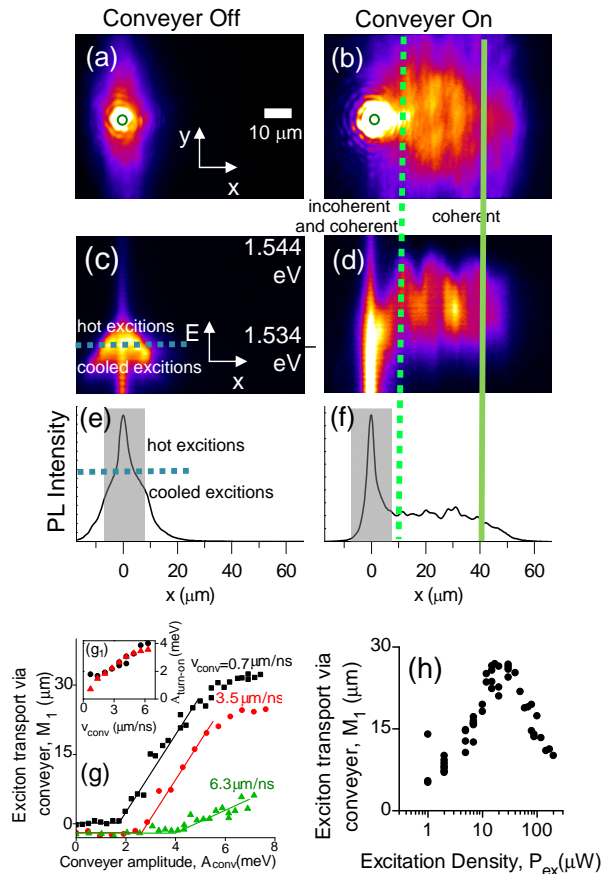


FIG. 1. The figures are taken from Ref. [9]. (a-d)  $x - y$  and  $x - \text{energy}$  PL images, and (e, f) PL intensity profiles  $I(x)$  for conveyor off and on here  $P_{\text{ex}} = 20 \mu\text{W}$ ,  $A_{\text{conv}} = 7.5 \text{ meV}$ ,  $v_{\text{conv}} = 0.7 \mu\text{m/ns}$ . The blue dashed lines in (c) and (e) are used to approximately separate the hot excitons near the center and the cooled excitons far from the center when the conveyor is off. The green dashed line across (b), (d) and (f) is used to indicate the hot (incoherent and coherent) excitons near the center and the coherent excitons far from the center when the conveyor is on. The green solid line across (b), (d) and (f) indicates the cooled excitons (degenerated excitons) traveling about  $40 \mu\text{m}$ . (g) The average transport distance of indirect excitons via conveyor  $M_1$  as a function of the conveyor amplitude,  $A_{\text{conv}}$ . Lines are a guide to the eye. The intersection point of the line is defined as  $A_{\text{turn-on}}$  where the dynamical localization-delocalization transitions occur as is shown in (g<sub>1</sub>).  $P_{\text{ex}} = 20 \mu\text{W}$ . (h) The measured average transport distance of indirect excitons via conveyor  $M_1$  as a function of density.  $A_{\text{conv}} = 4.9 \text{ meV}$ ,  $v_{\text{conv}} = 0.7 \mu\text{m/ns}$ .

The above experimental facts raise several interesting questions which need to be clarified. For example, whether the efficiency of the exciton transport for lower conveyor velocity is also related to the Chern number, or not [6]? The other important issue is whether the several bright stripes come from the exciton coherence or not. The excitons in the coherent state or the degenerate

state mean the off-diagonal long-range order exists in the system and the excitons are in a condensed state. Previously, a nonlinear Schrödinger equation including the attractive two-body interaction and the repulsive three-body interaction was proposed to explain the complex exciton patterns where the excitons are assumed to be in a coherent state [10–13]. One may ask naturally if the nonlinear Schrödinger equation can explain the exciton transport. In Ref. [9], the indirect excitons were considered as classical particles. The conveyor velocity and amplitude, as well as the exciton density, dependencies of the transport distances are all explained by a classical diffusion equation. However, the exciton degeneracy hidden in the PL patterns were not studied. As will be seen, the spatial and spectral patterns give the opportunity to coherence of the indirect excitons.

Since any realistic material inevitably contain a certain degree of impurities and defects, and the interactions between particles are almost always present, the combined effect of disorder and interactions can lead to novel quantum states such as the Bose glass phase in disordered Bosonic systems [14, 15]. Recently, the phase transition between the Bose glass and the superfluid was directly observed in the two-dimensional Bose glass in an optical quasicrystal [16]. The observed dynamical localization-delocalization transitions in conveyor for excitons gives another platform to answer more fundamental questions about the delocalization-localization transition [17].

By analysing the PL patterns, we find the exciton transport can be simplified as the diffusion of Bosons with the finite lifetime in a moving lattice. The main findings of this work are summarized as follow. (i) The pattern can be divided approximately into the incoherent part and coherent part which can be described by the diffusion differential equation used in Ref. [9] and the nonlinear Schrödinger equation proposed by us respectively. (ii) The bright stripes are the interplay between the coherent excitons and the moving lattices. (iii) The cooling rate is the key factor in the exciton transport. (iv) The lifetime and cooling rate of the coherent excitons are estimated. (v) The sample is very clean and free of impurity. We discuss the data and build a time-dependent nonlinear Schrödinger equation in Sec. II to describe the coherent excitons. We also show how to obtain the PL intensity profiles  $I(x)$  by calculating the escape rate. In Sec. III, numerical calculations and detailed discussions on the exciton distribution in moving lattices are given. Sec. IV is devoted to a brief summary.

## II. MODEL HAMILTONIAN

The clues of understanding the PL patterns in the conveyor belt come from the various exciton patterns found by the previous experiments, in particular, the two puzzling exciton rings, inner and external, and periodic bright spots in the external ring [8, 18, 19]. A charge-separated transport mechanism was proposed and gave

a satisfactory explanation both of the formation of the two exciton rings and of the dark region between the inner and the external ring [20, 21]. This mechanism was further confirmed by PL images of single quantum well [21].

As pointed out in Refs. [20, 21], when electrons and holes are first excited by high-power laser, they are actually charge-separated and have a small recombination rate. No true excitons are formed at this stage. They can travel a long distance from the laser spot before recombination. After a long-distance traveling, the hot electrons and holes collide with the semiconductor lattices and are cooled down. The cooled electrons and holes forms the excitons in the annular region near the the laser spot. The recombination of this part of excitons generates a PL ring. As the drift speed of electrons (with smaller effective mass) is larger than that of holes (with larger effective mass), there are always some electrons and holes escaping from this recombination. Also due to the neutrality of the coupled quantum wells, the negative charges will slow down and begin to accumulate at the sites far away from the PL ring. The cold electrons and holes then eventually meet to form the excitons. This part of the excitons recombine and also form the exciton ring at the boundary of the opposite charges. The second ring is far away the laser spot comparing with the former. The two rings were called as inner ring and external ring respectively.

As the excitons forming in the external ring are from the cooled electrons and holes, they have a low kinetic energy and temperature. While whether these excitons are condensed is in debate [20, 22–28], we reasonably assumed that the excitons were in the highly degenerated states, and proposed a self-trapped interaction model involving an attractive two-body interaction and a repulsive three-body interaction [10, 11, 13]. The mechanism gave a good account to the periodic bright spots in the external ring. In addition, it also explained well the abnormal exciton distribution in an impurity potential, in which the PL pattern became much more compact, and exhibited an annular shape with a darker central region [29]. Moreover, the model also captured some experimental details. For instance, the dip can turn into a tip at the center of the annular cloud when the sample was excited by a higher power lasers.

Inspired by both the above experimental data and theories, we are ready to investigate the exciton PL patterns in the moving lattices. As we know, the PL intensity is approximately proportional to the exciton number and the PL energy is approximately proportional to the exciton energy which includes the kinetic, the bound and the interaction energies. However, the bound energy remains unchanged due to the special structure of the spatially separated electrons and holes. The interaction energy between excitons is also negligible in the low-density case. As a result, the change of PL energy is only related to the kinetic energy. The PL energies shown in Fig. 1 (c) (1.534 eV marked by blue dashed line) and PL in-

tensities in Fig. 1 (e) far from the center are lower than those near the center. Therefore, it indicates that the excitons near the center have larger kinetic energy and higher particle density. We argue that the spatial distribution of excitons here is also consistent with that of the exciton rings reported in Ref. [8, 18]. The hot excitons are formed at the center [dark region  $-10 \mu\text{m} < x < 10 \mu\text{m}$  in Fig. 1 (e)] and the cooled excitons are located far from the center. So there exist two kinds of excitons, one is the hot excitons near the center and can be regarded as classical particles, the other is the cooled excitons far away the center cannot be regarded as classical particles.

When the conveyer is turned on [see Fig. 1 (b)], the moving potential modifies both the exciton potential energy and the PL energy [see Fig. 1 (d)]. While the moving lattices drag the hot excitons, they are cooled down further by inelastic collision to the semiconductor phonons. In comparison with the high temperature case near the center, the excitons far from the center have a long de Broglie wavelength in the low temperature region. As we know, a quantum phase transition occurs when the Bosons condense from the non-degenerate state to degenerate state. Whether the finite life-time excitons can experience a Bose-Einstein condensation transition is an interesting issue. Neglecting the above complexity, we roughly divide the exciton distribution into two parts by the green dashed line shown in Fig. 1 (b), (d) and (f). On the left side of the green dashed line, part of the excitons are in coherent state and part of excitons are in incoherent state. On the right side of the green dashed line, however, we consider all the excitons are in coherent states or degenerate states. According to the above analysis, the coherent excitons may come from two parts. One part directly comes from the hot exciton near the center by the cooling. The other comes directly from the pairing of the cooled electrons and holes.

It is useful to estimate the exciton parameters according to the above analysis. As is indicated by the green dashed line in Fig. 1, after a  $10 \mu\text{m}$  traveling, the hot excitons can become highly degenerated excitons. As is also marked by a blue solid line, after another  $30 \mu\text{m}$  traveling, the coherent excitons recombine. If the excitons follow the conveyor belt with a low velocity  $v_{\text{conv}} = 0.7 \mu\text{m}/\text{ns}$ , it takes about 14 ns for the hot excitons to the highly degenerated excitons. So the cooling time of the excitons from classical particles to coherent particles is about 14 ns. It takes another 40 ns before the degenerated excitons recombine. So the lifetime of the coherent excitons is estimated to be about 40 ns. This is the first time to obtain the lifetime of indirect exciton experimentally.

Based on the above analysis, it is reasonable to model the highly degenerate exciton gas by a time-dependent nonlinear Schrödinger equation [10, 13]

$$i \frac{d|\Psi(t)\rangle}{dt} = H |\Psi(t)\rangle, \quad (1)$$

where  $|\Psi\rangle = |\psi_1, \psi_2, \dots, \psi_L\rangle$  and  $L$  is the lattice length.

The tight-binding Hamiltonian reads

$$H = \sum_j \{ \tilde{t} (|\psi_j\rangle \langle \psi_{j+1}| + \text{h.c.}) + [V_{\text{conv},j}(t) + F(n_j) - i\gamma] |\psi_j\rangle \langle \psi_j| \}, \quad (2)$$

where

$$\begin{aligned} V_{\text{conv},j}(t) &= A_{\text{conv}} \cos [2\pi (j - v_{\text{conv}}t) / \lambda] \\ &= A_{\text{conv}} \cos (2\pi \kappa j - \omega t) \end{aligned} \quad (3)$$

denotes the moving external potential created by a set of ac gate voltages. When  $v_{\text{conv}} = 0$  and  $\omega = 0$ , the moving lattice reduces to the static lattice. The parameter  $\gamma = 1/\Gamma > 0$  is the loss rate and  $\Gamma$  is the exciton average lifetime.  $\tilde{t}$  is the hopping amplitude and is set to be 1 in the following discussions.  $n_j = |\psi_j|^2$  is the local probability density.  $F(n_j)$  is the effective interaction between the indirect excitons.

In general, the excitons are considered as the weak repulsive interactions  $F(n_j) = gn_j$ . Note that  $F(n_j) = -g_1 n_j + g_2 n_j^2$  was used to explain various exciton patterns [10–13]. The above phenomenological interaction may come from the dipolar interaction and the exchange interaction. Since the effective parameter  $g_1 \propto N$  and  $g_2 \propto N^2$  ( $N$  is the particle number), we have the relationship  $g_2 \propto g_1^2$ . We take  $g_2 = \epsilon g_1^2$  here  $\epsilon$  is the parameter describing the complex interactions. As will be seen in Sec. III B, the effects of these two kinds of interactions are identical except for the cases of the very low and very high particle density. Eq. (1) is the modified Gross-Pitaevskii equation when  $\gamma = 0$ . Unlike the Gross-Pitaevskii equation which is usually used to determine the ground states of a low-temperature Bosonic gas with a short- or zero-range two-body interaction, Eq. (1) contains the effect of the finite particle lifetime.

As the norm of the wavefunction decreases with time

$$\begin{aligned} \frac{d}{dt} I(t) &= \frac{d}{dt} \langle \Psi(t) | \Psi(t) \rangle = i \langle \Psi(t) | (H^\dagger - H) | \Psi(t) \rangle \\ &= -2\gamma \langle \Psi(t) | \Psi(t) \rangle = -2\gamma I(t), \end{aligned}$$

the time-dependent wavefunction norm can be written as

$$I(t) = \langle \Psi(t) | \Psi(t) \rangle = \sum_j |\psi_j(t)|^2 = \exp(-2\gamma t), \quad (4)$$

when the initial-state is normalized  $\langle \Psi(0) | \Psi(0) \rangle = 1$ .  $\gamma$  is the lost rate which is inversely proportional to the lifetime of the excitons. We define the escaping probability at location  $j$  of the walker as

$$I_j = 2\gamma \int_0^\infty dt |\psi_j(t)|^2, \quad (5)$$

which satisfies  $\sum_j I_j = \sum_j 2\gamma \int_0^\infty dt |\psi_j(t)|^2 = \int_0^\infty dt I(t) = 1$ .  $I_j$  is the summation of luminescence intensity of all the exciton states and is the PL intensity profile.

The cooling of the excitons is another important physical factor in the exciton diffusion. With the increase of the time, the high-energy excitons relax to low-energy excitons and condense to their degenerate states. The condensed excitons in the confined well occupied the highly degenerate states can be further cooled before recombination. The cooling process can be well simulated by the imaginary time evolution. As we know, for a stationary state or eigenstate, if the time  $t$  is artificially replaced by  $-it$ , the wavefunction will exponential decay in its time evolution. According to the superposition principle, a state can be expanded as the linear superposition of all the eigenstates. In the imaginary time evaluation of the state, the components with the higher eigen energies have the faster decay rates which is equivalent to the relaxation of high energy components to the low energy components [30]. Although the energy levels are not well defined in the time-dependent non-Hermitian system, the energy levels have previously been observed in previous experiments [8, 18, 19, 29, 31] and investigated theoretically [10–13, 32]. We use the imaginary time-evolution of the Schrödinger equation in Eq. (1) to describe the cooling process.

In the following calculations, we solve the time-dependent Schrödinger equation (1) in a real time interval  $\Delta t$  with the initial state  $\Psi(0)$  to obtain the time evolution state  $\Psi(\Delta t)$ . Then the state  $\Psi(\Delta t)$  is used as the initial state, we solve the time-dependent Schrödinger equation (1) in a imaginary time interval  $i\Delta t'$  to obtain the time evolution state  $\Psi(\Delta t + i\Delta t')$ . At last, the wavefunction  $\Psi(\Delta t + i\Delta t')$  is normalized as [30]

$$I(\Delta t + i\Delta t') = |\Psi(\Delta t + i\Delta t')|^2 = \exp(-2\gamma\Delta t). \quad (6)$$

Repeating the above process  $\mathcal{N}$  times until  $I(\mathcal{N}[\Delta t + i\Delta t']) \sim 0$ , we get a serial of  $\Psi(n[\Delta t + i\Delta t'])$  to calculate  $I_j = 2\gamma \sum_{n=0}^{\mathcal{N}} |\Psi(n[\Delta t + i\Delta t'])|^2$ . We define  $\tau = \Delta t' / \Delta t$ . The larger  $\tau$  indicates the longer cooling time. So  $\tau$  is proportional to cooling speed.

It should be emphasized that the method above is effective since the normalization condition of the escape rate  $I_j$  in Eq. (5) guarantees the convergence of the calculations. Otherwise, without considering the time-dependent normalized condition, the propagation of a wave-packet still meets the boundary and reflects under the open boundary condition. Even though the absorbing boundary condition is adopted, the boundary also have a great effect on the evolution of the wavefunction. In such a case, the interference fringes are formed by interference between incident and reflected waves and no convergent solution can be obtained.

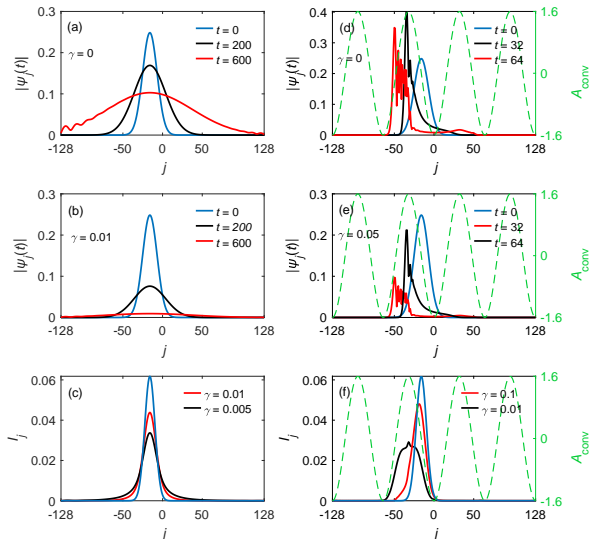


FIG. 2. The wave packet diffusion without a periodic potential (left column) and with the static periodic potential (right column). The free diffusion of a wave packet at different time without the dissipation  $\gamma = 0$  (a) and with the dissipation  $\gamma = 0.01$  (b). The diffusion of a wave packet modulated by the static periodic potential (dashed line) at different time without the dissipation  $\gamma = 0$  (d) and with the dissipation  $\gamma = 0.05$  (e).  $I_j$  distribution for the different dissipation  $\gamma$  for the free diffusion (c) and for the diffusion modulated by the static periodic potential  $V_{\text{conv},j}$  (f). The parameters of the periodic potential in Eq. (3) are set as  $A_{\text{conv}} = 1.6$ ,  $\omega = 0$ , and  $\lambda = 64$ .

### III. NUMERICAL ANALYSIS

#### A. A wave packet diffusion: without particle interactions

According to the above analysis, there are various sources for the coherent excitons. As a result, the initial distribution of the degenerate excitons can be considered as a wave packet with multi-peaks. In order to understand the transport of the wave packet, let us first study the simplest case of the diffusion of a wave packet with one-peak. We solve the time-dependent nonlinear Schrödinger equation (1) in real-time only under the open boundary condition ( $\psi_{\pm L} = 0$ ) for an initial Gauss wave packet  $\psi_j(0) = \sqrt{(2\kappa/\pi)} \exp[-\kappa(j - j_0)^2]$ . The results with the parameters  $j_0 = -16$ ,  $\kappa = 0.006$  and  $L = 128$  are shown in Fig. 2. In the following discussions, the blue lines in all the figures indicate the shape of the initial wave packet.

The physics of the wave packet diffusion is very simple [33, 34]. For the Gauss wave packet, its wave functions both in real space and momentum space are all of the Gauss type. According to the uncertainty relation  $\Delta x \Delta p \approx \hbar$ , with the increase of time, the larger  $\Delta x$  leads to the smaller  $\Delta p$ , here  $\Delta x$  and  $\Delta p$  are the full

width at half maximum of the Gauss wave packet. If we approximately take  $v \approx \Delta v$ , the smaller  $\Delta p$  leads to the lower the propagation speed. As a result, although the diffusion becomes slower and slower as the time increases, the wave finally arrives at the boundary and is reflected. Interference fringes are generated by the interference between reflected and incident waves. The above statements are true whether it is without the periodic potential in Fig. 2 (a) or with the static periodic potential in Fig. 2 (d). The difference is that more interference fringes appear in Fig. 2 (d) due to the interplay between the wave and the periodic potential. When we take the dissipation of the particles into account, the wave packet decays in Fig. 2 (b) and (e) with the time goes on. The escape probability  $I_j$  in Eq. (5) is calculated and shown in Fig. 2 (c) and (f). As expected, the particle dissipation suppresses the wave packet diffusion. From Fig. 2 (f),  $I_j$  can be deviated from the initial position due to the modulation of the external potential.

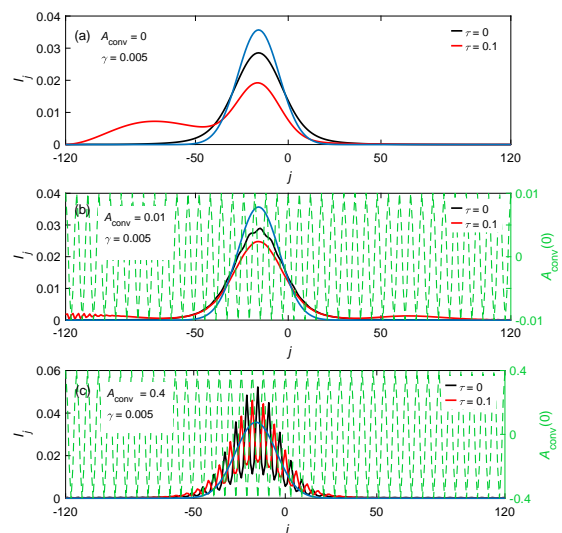


FIG. 3. The wave packet diffusions without the cooling [black lines] and with the cooling [red lines] modulated by the static periodic potentials with the different intensities (a)  $A_{\text{conv}} = 0$ , (b)  $A_{\text{conv}} = 0.01$  and (c)  $A_{\text{conv}} = 0.4$ .

We next investigate the cooling effect on the wave packet diffusion. The time-dependent nonlinear Schrödinger equation (1) is solved with the real-time and imaginary-time evolutions alternatively to obtain the escape rate  $I_j$  of the coherent excitons. The result of  $I_j$  is shown in Fig. 3. It can be seen that the cooling helps the wave packet diffusion. We can understand the underlying physical picture as follow [33, 34]. A wave packet in free space can be considered as the superposition of the plane waves with the different wave vectors. When the condensed Bosons are considered to be in a state of Gauss wave packet in momentum space, their distribution in the Cartesian coordinate space is still Gauss type. With the time increases, the wave packet will spread in

coordinate space and will contract in momentum space. However, their waves are still Gauss types. With the temperature decreases, the low-energy probability of the Gauss wave packet increases accordingly since the wave packet in momentum space is modulated by the factor  $\exp(-\beta E_k)$  ( $E_k = k^2/2$ ). The narrower the wave packet in momentum space, the wider wave packet in coordinate space [33, 34]. As a result, the quantum mechanical effect is in opposition to the classical effect where the spreading of classical particle becomes slow with the decrease of the temperature.

By comparing the black lines and the red lines in Fig. 3 (b), it is found that the cooling also helps the wave packet spread in a static periodic potential. The physical picture can also be understood in a similar way. In the static periodic potential, the eigenfunction of a particle is the Bloch wave which can be expanded in terms of the Wannier functions. Correspondingly, the energy bands come from the splitting of the degenerate energy levels. A wave packet in periodic potential can be considered as a superposition of the Bloch waves with the different wave vectors. With time increasing and particle cooling, the particle probabilities in low-energy bands increase accordingly. The narrower the wave packet in momentum space, the wider the wave packet in coordinate space. As a result, the cooling enhances the diffusion of the wave packet.

It is interesting to see in Fig. 3 (c) that the peaks of the  $I_j$  for  $\tau > 0$  are located at the crests of the periodic potential, which is in contrast to the case of  $\tau = 0$  where the peaks are located at the troughs. The reason can be understood as follows. According to the above analysis, with the lowering of the temperature, the Bosons tend to condense at  $k = 0$ , which results in the increasing of  $\Delta x$ . In the large  $A_{\text{conv}}$  case, the Wannier functions are the atomic orbital wavefunctions in a unit cell and the particles are confined in a single unit cell. The stronger the confinement, the larger the  $\Delta x$ . The particles tend to move to the boundary of the unit cell to obtain the large  $\Delta x$  which causes the dip of particle distribution at the center of the unit cell. This quantum behavior can be used to detect the exciton degeneracy.

The wave packet diffusion in a moving lattice is shown in Fig. 4. The moving lattice modifies the shape of the Gauss wave packet. With the increase of the time, the wave packet follows the moving lattice while its height decreases obviously due to the finite lifetime of the exciton [Fig. 4 (a) and (b)]. The exciton cooling ( $\tau = 0.5$ ) in Fig. 4 (b) dramatically increases the transport distance in comparison with the case without the cooling ( $\tau = 0$ ) in Fig. 4 (a). The escaping probability  $I_j$  corresponding to the case in Fig. 4 (a) and (b) is presented in Fig. 4 (c). The average transport distance  $M_1$  increases with the cooling parameter  $\tau$  and then tends to saturation as is shown in Fig. 4 (d). We can conclude that the cooling is the key factor to the exciton transport via the conveyor.

The reason can be understood from the case of the low velocity and the high  $A_{\text{conv}}$  of the moving periodic po-

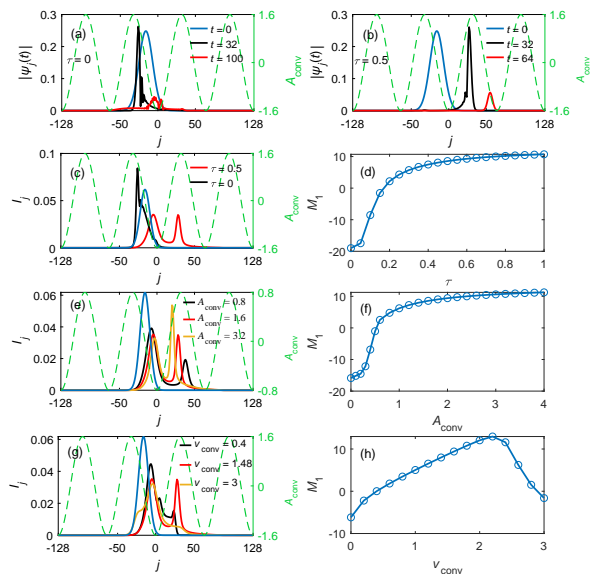


FIG. 4. The wave packet diffusions in a moving lattice without considering the cooling (a) and considering the cooling (b).  $I_j$  of the two cases of (a) and (b) are given in (c). (e) and (g) show  $I_j$  with the different moving lattice intensity  $A_{\text{conv}}$  and moving speed  $v_{\text{conv}}$ . The cooling speed  $\tau$ , the lattice intensity  $A_{\text{conv}}$  and the lattice velocity  $v_{\text{conv}}$  dependencies of the transport distant  $M_1$  are shown in (d), (f) and (h) respectively. The parameters used in all figures are:  $A_{\text{conv}} = 1.6$ ,  $v_{\text{conv}} = 1.48$ ,  $\gamma = 0.05$ .

tential. In such case, the Bloch theory can be assumed to be correct approximately and the Wannier functions can be approximated as the atom-orbital functions (particle wave functions in unit cell). The overlap of the neighbouring low orbital functions is less than that of the high orbital functions. The little overlap of the neighbouring low orbital functions leads to the little tunneling between unit cells. With the cooling, the excitons tend to occupy the low energy bands. The occupation probability of the low orbital state increases with the cooling parameters  $\tau$ . With increase of the cooling further, most part of the particles are in the low orbital state. As a result, the particles follow the moving lattice. So the change of the average transport distance  $M_1$  obvious increase with  $\tau$  as is shown in Fig. 4 (d).

The tunneling between unit cells decreases with the increase of the lattice height  $A_{\text{conv}}$ . In the high  $A_{\text{conv}}$  case, the tunneling between unit cells is inconspicuous. So the transport distance increases with the  $A_{\text{conv}}$  and then tends to saturation as is shown in Fig. 4 (e). In the low lattice speed case, the average transport distance  $M_1$  increases with the lattice speed as is shown in Fig. 4 (h), which indicates the exciton transport follows the moving lattices. In the high lattice speed case, the energy band theory breaks down. It is definitely that the tunneling between the unit cells decreases with the increase of the lattice speed which is adverse to the particles transport.

We therefore argue that the particles follow the moving lattices only in the low velocity and high lattice amplitude cases.

### B. A wave packet diffusion: with particle interactions

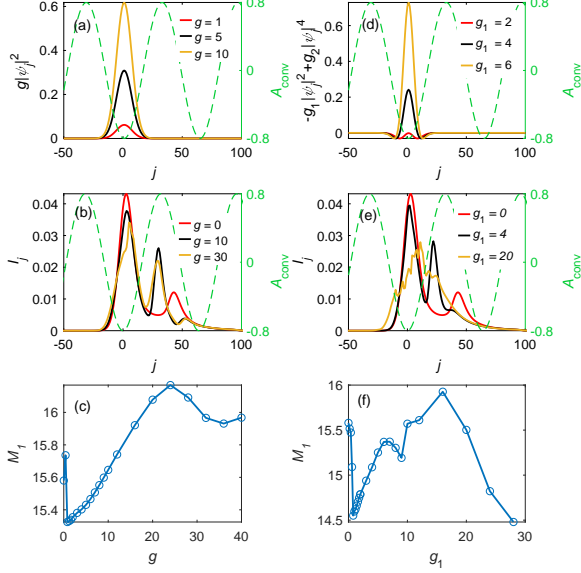


FIG. 5. The wave packet diffusions of the weak repulsive particles. The following parameters are used in the numerical analysis:  $A_{\text{conv}} = 0.8$ ,  $v_{\text{conv}} = 2.08$ ,  $\tau = 0.5$  and  $\gamma = 0.05$ . For the pure repulsive case, the interaction parameter  $g$ -dependent effective potential  $g|\psi_j|^2$ , the distribution patterns  $I_j$  with different  $g$  and transport distance  $M_1$  as a function of  $g$  are given in (a), (b) and (c) respectively. For the complex interaction  $-g_1|\psi_j|^2 + g_2|\psi_j|^4$  case, we set  $g_2 = \epsilon g_1^2$  and  $\epsilon = 8$ . The interaction parameter  $g_1$ -dependent effective potential, the distribution patterns  $I_j$  with the different  $g_1$  and transport distance  $M_1$  as a function of  $g_1$  are given in (d), (e) and (f) respectively.

In general, the excitons are considered to have the weak repulsive interactions. We study the exciton transport with this kind of interactions in Figs. 5 (a), (b) and (c). The interaction  $g|\Psi_j|^2$  acts as the effective potential as is shown in Fig. 5 (a) with a different strength  $g$ .  $I_j$  with the different  $g$  is shown in Fig. 5 (b). It indicates that the interactions have a significant effect on the particle transport.  $M_1$  as a function of  $g$  is shown in Fig. 5 (c). Two different effects affect the particle transport for the repulsive interactions. One is that the repulsive interactions always favor the particle spreading. The other is that the repulsive interactions modify the lattice intensity equivalently, which is detrimental to particle transport. So the particle transport  $M_1$  is a non-monotonic function of  $g$ .

We have phenomenally proposed the two-body attractive and three repulsive interactions to understand the

exciton patterns. To study how the complex interactions modify the exciton transport, we show the result with the effective interaction potential  $-g_1|\psi_j|^2 + g_2|\psi_j|^4$  in Fig. 5 (d). Here  $g_2 = \epsilon g_1^2$  with  $\epsilon = 8$ . For the large  $g_1$  cases, the excitons are in repulsive interactions as that in Fig. 5 (a). So  $I_j$  in Fig. 5 (e) and  $M_1$  in Fig. 5 (f) are similar to those of Fig. 5 (b) and  $M_1$  in Fig. 5 (c) respectively.

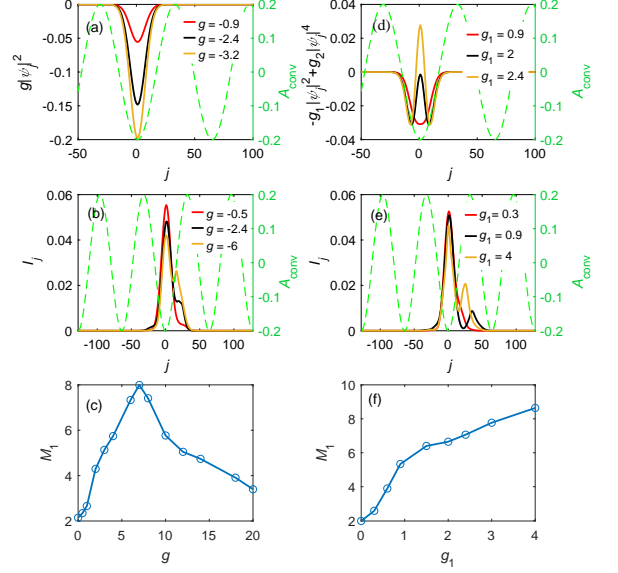


FIG. 6. The wave packet diffusions of the attractive particles. The following parameters are used in the numerical analysis:  $A_{\text{conv}} = 0.2$ ,  $v_{\text{conv}} = 2.08$ ,  $\tau = 0.5$  and  $\gamma = 0.05$ . For the pure attractive case, the interaction parameter  $g$ -dependent effective potential  $-g|\psi_j|^2$ , the distribution patterns  $I_j$  with different  $g$  and transport distance  $M_1$  as a function of  $g$  are given in (a), (b) and (c) respectively. For the complex interaction  $-g_1|\psi_j|^2 + g_2|\psi_j|^4$  in the weak attractive interaction region, we set  $g_2 = \epsilon g_1^2$  and  $\epsilon = 8$ . The interaction parameter  $g_1$ -dependent effective potential, the distribution patterns  $I_j$  with the different  $g_1$  and transport distance  $M_1$  as a function of  $g_1$  are given in (d), (e) and (f) respectively.

In the low exciton density case,  $-g_1|\psi_j|^2 + g_2|\psi_j|^4$  is in the attractive interaction region. It is interesting to study how the attractive interactions  $-g|\psi_j|^2$  and  $-g_1|\psi_j|^2 + g_2|\psi_j|^4$  modify the particle transport. We present the effective attractive interactions in Figs. 6 (a) and (d). In order to study the effects of the weak interaction more clearly, a small lattice intensity  $A_{\text{conv}} = 0.2$  is adopted. This is in contrast to the repulsive case shown in Figs. 5 (a) and (d) [ $A_{\text{conv}} = 0.8$ ]. In the pure attractive case  $-g|\psi_j|^2$ , a wave packet will collapse in the time evolution as is shown in Fig. 6 (b). However, the finite exciton lifetime prevents the pocket from collapsing further.

The attractive interactions also have two effects on particle transport. One is that the attractive interactions always hinder the particle spread. The other is that the increase of the effective lattice intensity facilitates the

particle transport. So the particle transport  $M_1$  is also a non-monotonic function of  $g$  [see Fig. 6 (c)]. In the small  $g_1 < 4$  case, the weak complex interactions are in the attractive region, which also modify the exciton transport in Fig. 6 (e) and (f). However,  $M_1$  shows a monotonic variation as a function of  $g_1$ .

### C. The disorder effects

The data of the exciton transport distance  $M_1$  via conveyer as a function of the conveyer amplitude  $A_{\text{conv}}$  are given in Fig.1 (g). It shows that the exciton cloud extension  $M_1$  is not affected by the motion of a shallow conveyer. Across the transition point however, the exciton cloud starts to follow the conveyer, and  $M_1$  increases with the increase of  $A_{\text{conv}}$ . At higher conveyer amplitude,  $M_1$  tends to saturation. As we know, the random disorders or impurities exist inevitably in the coupled quantum well grown with molecular beam epitaxy. The destructive interference of scattered waves due to the strong disorders leads to the Anderson localizations [35, 36]. As a result, the experimental data is naturally explained as the dynamical localization-delocalization transition. The dynamical localization was found in two-band system driven by the DC-AC electric field, in which the Rabi oscillation is quenched under the certain ratio of Bloch frequency and AC frequency [37, 38]. An interesting issue here is whether the data can really be explained by the dynamical localization or not.

The Anderson localizations are generally studied with indirect method where the random disorders are simulated by a quasiperiodic on-site modulation [39, 40]. The quasiperiodic potential is set to be site dependent, i.e.

$$V_{\text{dis},j} = 2A_{\text{dis}} \cos(2\pi\alpha j),$$

with  $A_{\text{dis}}$  being the strength,  $\alpha$  being an irrational number which is used to characterize the quasiperiodicity. The irrational number is usually taken as the value of the inverse of golden ratio [ $\alpha = (\sqrt{5} - 1)/2$ ]. The value is closely related to the Fibonacci number which is defined by  $F_n/F_{n+1}$  where the Fibonacci sequence of numbers  $F_n$  is defined using the recursive relation with the seed values  $F_0 = 0$ ,  $F_1 = 1$  and  $F_n = F_{n-1} + F_{n-2}$  [40, 41]. The merit of using Fibonacci numbers is that the quasiperiodic potential  $V_{\text{dis}}(j + F_{n+1}) = V_{\text{dis}}(j)$  becomes periodic.

To simplify the discussion, the particle interaction, lifetime and cooling are not taken into account. The Hamiltonian in Eq. (2) can be written as

$$H(t) = \sum_j [\tilde{t}(|\psi_j\rangle\langle\psi_{j+1}| + \text{h.c.}) + \mathcal{V}_j(t)|\psi_j\rangle\langle\psi_j|], \quad (7)$$

here  $\mathcal{V}_j(t) = V_{\text{conv},j}(t) + V_{\text{dis},j}$ , which is a spatial periodic  $\lambda F_{n+1}$  and time periodic  $T$  function  $\mathcal{V}_j(t) = \mathcal{V}_j(t + T) = \mathcal{V}_{j+\lambda F_{n+1}}(t)$  here  $\lambda$  is an integer. The time dependence of the Hamiltonian (7) leads to no stationary states in

the system. However, the Hamiltonian (7) has the time periodicity. We can write the state as

$$|\psi_j(t)\rangle = e^{-i\varepsilon t} |c_j(t)\rangle,$$

where  $\varepsilon$  is the quasienergy and  $|c_j(t)\rangle = |c_j(t + T)\rangle$  is periodic function which satisfies the time-dependent equation

$$[H(t) - i\partial_t] |c_j(t)\rangle = \varepsilon |c_j(t)\rangle$$

according to the Floquet theorem [38, 42]. As  $e^{i\varepsilon(t+T)} = e^{i\varepsilon t}$ , it requires the quasienergy satisfies  $\varepsilon_l = \frac{2\pi l}{T} = \omega l$  where  $l$  is an integer. To ensure the consistency between the Floquet theorem and the Bloch theorem in the form, the period is assumed to be  $T = Na$  and the quasienergy is confined in the first time Brillouin zone  $]-\pi/a, \pi/a]$ , with  $a$  being the time unit.  $]-\pi/a, \pi/a]$  means an excluded value  $-\pi/a$  on the left and included  $\pi/a$  on the right. As a result,  $l$  can be taken as  $]-N/2, N/2]$ . From the time-dependent nonlinear Schrödinger equation, the Hamiltonian in Eq. (7) can be transformed to a tight-binding Floquet operator in the second quantization form

$$\mathcal{H}(t) = \sum_j \left[ \tilde{t} \left( c_j^\dagger(t) c_{j+1}(t) + \text{h.c.} \right) + c_j^\dagger(t) (\mathcal{V}_j(t) - i\partial_t) c_j(t) \right]. \quad (8)$$

After the Fourier transform

$$c_j(t) = N^{-1/2} \sum_{n=-N/2}^{N/2} c_{j,n} e^{i\omega n t},$$

$$c_j^\dagger(t) = N^{-1/2} \sum_{n=-N/2}^{N/2} c_{j,n}^\dagger e^{-i\omega n t},$$

and the inner product  $\langle\langle \mathcal{H}(t) \rangle\rangle = \frac{1}{T} \int_0^T \mathcal{H}(t) dt = \frac{1}{N} \sum_{n=-N/2}^{N/2} \mathcal{H}(n)$ , the time-dependent Floquet operator  $\mathcal{H}(t)$  becomes [42, 43]

$$\mathcal{H} = \sum_{j,n} \left\{ \left( \tilde{t} c_{j,n}^\dagger c_{j+1,n} + A_{\text{conv}} e^{-i2\pi n j} c_{j,n-1}^\dagger c_{j,n} + \text{h.c.} \right) + [A_{\text{dis}} \cos(2\pi\alpha j) - n\omega] c_{j,n}^\dagger c_{j,n} \right\}. \quad (9)$$

It is obviously that several sub-bands forming for different  $n$  of the model (9). For a given  $n$ , the model (9) can be mapped to Harper model which is the two-dimensional electron gas in a magnetic field if  $\eta$  is regarded as a magnetic flux penetrating the unit cell [44].

Under the Floquet ansatz  $\langle\langle c_{j,n}^\dagger(t) c_j(t) \rangle\rangle = \sum_n c_{j,n}^\dagger c_{j,n}$ , we can define a time-average inverse of the participation ratio (TMIRP) of the normalized eigenstate  $|c_{j,n}\rangle_l$  corresponding to the eigenvalue  $\varepsilon_l$ ,

$$\text{TMIRP}_l = \sum_{j,n} \left| \langle c_{j,n}^\dagger | c_{j,n} \rangle_l \right|^4.$$

The localization of the whole system can be characterized by the average of TMIPR

$$\overline{\text{TMIPR}} = \sum_l \text{TMIPR}_l / L.$$

For a delocalization phase of the system,  $\overline{\text{TMIPR}}$  is of the order  $1/L$ , whereas it approaches 1 in the localized phase.

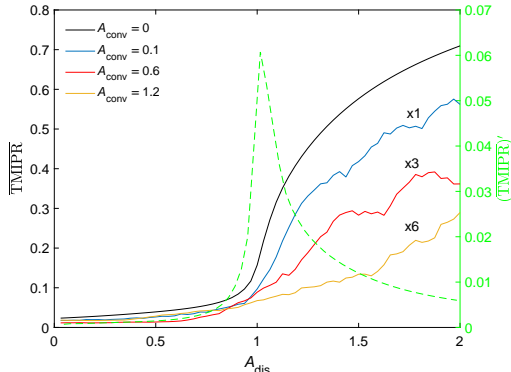


FIG. 7. The  $\overline{\text{TMIPR}}$ 's dependence on  $A_{\text{dis}}$  for different  $A_{\text{conv}}$ . The data have been expanded three and six times for the cases of  $A_{\text{conv}} = 0.6$  and  $1.2$ . The green dashed line is the slope of black line and is used to show the phase transition occurring at  $A_{\text{dis}} = 1$  for the AAH model ( $A_{\text{conv}} = 0$ ). The parameters used in the numerical calculation are  $L = N = 65$ ,  $\alpha = 0.2$  and  $\omega = 0.5$ .

We diagonalize the time-mean tight-binding Hamiltonian (9) to get the eigenstates  $|c_{j,n}\rangle_l$  for calculating  $\overline{\text{TMIPR}}$ . The result is shown in Fig. 7. In the case of  $A_{\text{conv}} = 0$ , the Hamiltonian (7) is reduced to the Aubry-André-Harper (AAH) model [44, 45]. The  $A_{\text{dis}}$  dependence of  $\overline{\text{TMIPR}}$  and its first derivative  $(\overline{\text{TMIPR}})' = d(\overline{\text{TMIPR}})/d(A_{\text{dis}})$  are shown in Fig. 7 by the black line and the green dashed line, respectively. A peak is found at  $A_{\text{dis}} = 1$  which is consistent with that of the AAH model where the Anderson localization transition occurs at  $A_{\text{dis}} = \tilde{t}$ . It indicates the effectiveness of the time-mean method. We further calculate the  $A_{\text{dis}}$  dependence of  $\overline{\text{TMIPR}}$  for different  $A_{\text{conv}}$ . Similar to the above research, for a wave packet driven by the moving lattices, the wave packet spreads over time, and tends to delocalization. For a wave packet driven by the random lattice, it tends to localize. As a result, the interplay of the two lattices leads to suppression of the  $\overline{\text{TMIPR}}$  with the increase of  $A_{\text{conv}}$ . As we know, when there is a competition between localization and delocalization in particular, a localization-delocalization transition usually occurs. It is surprising that no visible localization-delocalization transition is found in the  $A_{\text{dis}}$  dependence of  $\overline{\text{TMIPR}}$  in Eq. (7) for the case of  $A_{\text{conv}} \geq 0.6$ .

The localization-delocalization transition can also be captured by the asymptotic behavior over long time of

the second-order moment of position operator  $\sigma^2(t)$  defined by the wave spreading [46–48]

$$\sigma^2(t) = \sum_j \langle c_j(t) | j^2 | c_j(t) \rangle,$$

with the initial localized state  $|c_j(0)\rangle = \delta_{j,0}$ . It gives the opportunity to further check the non-existence of the localization-delocalization transition. The asymptotic spreading of  $\sigma^2(t)$  is described by the power law, i.e.  $\sigma^2(t) \sim t^{2\delta}$  where  $\delta$  is the diffusion exponent. In terms of dynamical behavior of a wave packet, measured by the exponent  $\delta = \delta(A_{\text{dis}})$ , the phase transition is discontinuous since  $\delta(A_{\text{dis}}) = 1$  for  $A_{\text{dis}} < \tilde{t}$  (ballistic transport),  $\delta(A_{\text{dis}}) \simeq 1/2$  at the critical point  $A_{\text{dis}} = \tilde{t}$  (almost diffusive transport), and  $\delta(A_{\text{dis}}) = 0$  in the localized phase  $A_{\text{dis}} > \tilde{t}$  (dynamical localization). When the spreading velocity  $v(A_{\text{dis}}) \sim \sigma(t)/t$  is further defined, the phase transition turns out to be smooth, with  $v(A_{\text{dis}})$  being continuous function of potential amplitude  $A_{\text{dis}}$  and  $v(A_{\text{dis}}) = 0$  for  $A_{\text{dis}} \geq 0.6$ .

We still use the above method to characterize the dynamical localization. We solve the time-dependent nonlinear Schrödinger equation of the Hamiltonian (7) with the initial localized state  $|c_j(0)\rangle = \delta_{j,0}$  to obtain  $|c_j(t)\rangle$  and  $v(A_{\text{dis}})$ . The dependence of  $v(A_{\text{dis}})$  on  $A_{\text{dis}}$  is shown in Fig. 8. For the case of  $A_{\text{dis}} = 0$ , the Hamiltonian in Eq. (7) is reduced to the AAH model. The dependence of  $A_{\text{conv}}$  on  $v(A_{\text{dis}})$  [black line] shows a transition at  $A_{\text{dis}} = 1(\tilde{t})$  obviously. With the applying of the moving lattices, either increasing its intensity  $A_{\text{conv}}$  [ $v_{\text{conv}}$  unchanged] in Fig. 8 (a) or increasing its velocity  $v_{\text{conv}}$  [ $A_{\text{conv}}$  unchanged] in Fig. 8 (b), the spreading velocity  $v(A_{\text{dis}})$  is suppressed. The most obvious feature is the disappearance of the delocalization-localization transition. We also calculate the conveyor amplitude  $A_{\text{conv}}$ 's dependence on  $M_1$  for the different disorder intensity  $A_{\text{dis}}$  [ $v_{\text{conv}} = 2.02$ ] in Fig.8 (c) and for the different conveyor velocity  $v_{\text{conv}}$  [ $A_{\text{dis}} = 1.6$ ] (d). Recalling the behavior of  $\overline{\text{TMIPR}}$  in Fig. 7, we therefore argue that the moving lattice breaks the Anderson localization transition.

#### D. Comparing the theory with the experiments

After detailed investigations of the various effects on the diffusion of a wave packet in the moving lattice, we are ready to study the experimental data. According to the discussions in sec. III C, the plateaus can not be explained by delocalization-localization transition due to the disorders, even though the disorders suppress the wave-packet transport. The disorders are firstly neglected in following numerical calculations. In addition, as the coherent excitons have different origins, the wave function of the coherent excitons was assumed with two peaks initially. The motivation of the two peaks comes from the two rings reported in Refs. [8, 18]. We solve the time-dependent nonlinear Schrödinger equation (1) with the initial wave function [black line in Fig. 9] to obtain

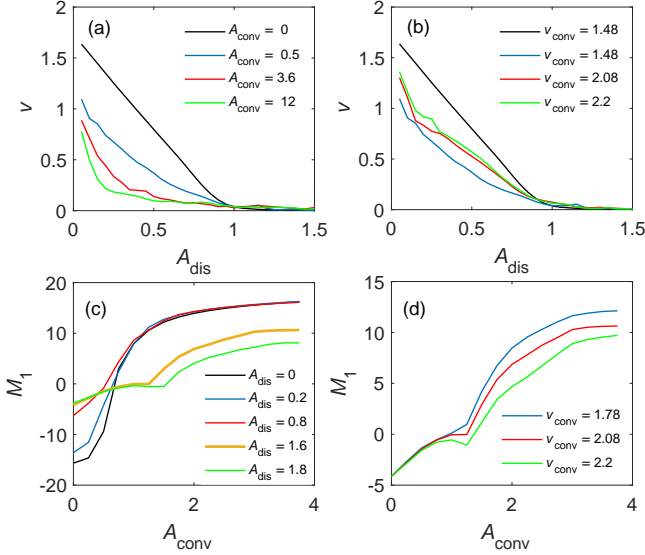


FIG. 8.  $v$  as a function of the disorder amplitude  $A_{\text{dis}}$  for the largest propagation time  $t = 150$  where in (a) the speed of the moving lattice is set to be  $v_{\text{conv}} = 1.48$  and in (b) the disorder amplitude is set to be  $A_{\text{conv}} = 1.6$  respectively.  $M_1$ 's dependence on the conveyer amplitude  $A_{\text{conv}}$  for the different disorder intensity  $A_{\text{conv}}$  [ $v_{\text{conv}} = 2.02$ ] (c) and for the different conveyer speed  $v_{\text{conv}}$  [ $A_{\text{conv}} = 1.6$ ] (d). The other parameters  $\gamma = 0.05$  and  $\tau = 0.5$ .

$I_j$  [red line in Fig. 9 (a)]. The appearance of the four peaks is basically consistent with the interference fringe.

The conveyer amplitude  $A_{\text{conv}}$ 's dependence on  $M_1$  is shown in Fig. 9 (b) for different  $v_{\text{conv}}$ . It indicates that the transport distance  $M_1$  increases with the conveyer amplitude  $A_{\text{conv}}$ . However, the exciton transport is less efficient for higher velocity. We also study the low-velocity case [green line] and find that the exciton transport is also less efficient for lower velocity. It indicates that the effective transport occurs at moderate conveyer speed.

Although no disorders are involved in the potential, the plateau can still be found in the low moving lattice amplitude  $A_{\text{conv}}$ . In particular, the plateau width increases with the conveyer velocity  $v_{\text{conv}}$  [see Fig. 9 (b<sub>1</sub>)]. This is consistent with the experimental data [given by black points in Fig. 1 (g)] where  $A_{\text{turn-on}}$  [defined as  $A_{\text{conv}}$  at the line intersection] increases with  $v_{\text{conv}}$ . The result with the disorders is shown in Fig. 9 (c), it is interesting to see that the plateau is destroyed with the increase the disorder intensity  $A_{\text{dis}}$ . We therefore believe that the plateau cannot be caused by the dynamical localization-delocalization transitions due to the disorders. We infer that the experimental sample is very clean. Their random potential strength is very weak, even if impurities exist.

According to the discussion in sec. III B, there is no difference between  $g|\psi_j|^2$  and  $-g_1|\psi_j|^2 + g_2|\psi_j|^4$  in describing the exciton interactions except for the case of the

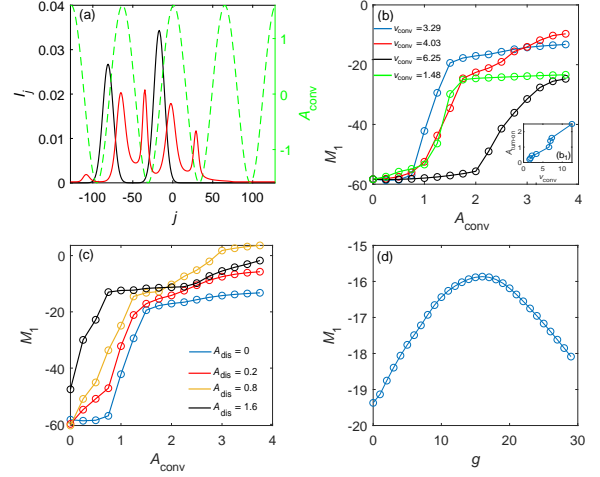


FIG. 9. (a) Red line: the PL intensity profile  $I_j$ . Black line: the initial wave-packet. Green-dashed line: the initial conveyer. The parameters  $v_{\text{conv}} = 1.48$  and  $A_{\text{conv}} = 1.6$  are used in the calculations. (b)  $M_1$  as a function of the conveyer amplitude  $A_{\text{conv}}$  for the different conveyer velocity  $v_{\text{conv}} = 1.48, 3.29, 4.03$  and  $6.25$  respectively. (b<sub>1</sub>)  $A_{\text{turn-on}}$  versus the conveyer velocity  $v_{\text{conv}}$ . (c)  $M_1$  as a function of the interaction parameter  $A_{\text{conv}}$ . (d)  $M_1$  as a function of the interaction parameter  $g$  with the parameters  $v_{\text{conv}} = 4.03$ ,  $A_{\text{conv}} = 2.5$ . The other parameters in these calculations are set as  $g = 1.2, \tau = 0.5$  and  $\gamma = 0.05$ .

very low particle density. We use the interaction  $g|\psi_j|^2$  to calculate the  $g$  dependence of  $M_1$  as is shown in Fig. 9 (d). The transport distance  $M_1$  increases firstly and then decreases with  $g$ . The behavior is similar to the experimental data in Fig. 1 (h) where the exciton transport via conveyer  $M_1$  increases firstly and then decreases with the excitation power  $\log(P_{\text{ex}})$ . As  $g \propto N$  when the wave function  $\psi_j$  is normalized, it indicates that the coherent exciton number  $N \propto \log(P_{\text{ex}})$ . We therefore infer that it is less efficient to increase the coherent exciton number by increasing the laser power  $P_{\text{ex}}$ . The cooling speed and long lifetime are still the key factors.

#### IV. SUMMARY

In summary, we have investigated the experimental data of electrostatic conveyor belt for excitons to understand the dynamical behaviors. We found that the formation of exciton patterns come from both the spatially-separated hot excitons and cooled excitons. The hot excitons can be regarded as classical particles whose transport can be well described by the classical diffusion equation. However, the cooled excitons are the coherent Bosons which must be described by the Schrödinger equation. The studies capture the nature of the exciton diffusion in conveyor belt, i. e. the excitons are cooled down during the transport. In particular, the excitons

are in highly degenerate states far from the laser spot, and their temperature becomes lower and lower. This is why the method of the real-time and imaginary-time evolution of the Schrödinger equation can give a good account of the spatial separation patterns. Even though some discrepancies exist between the theory and experiment, the numerical results are expected to be realized in the further.

By calculating the distribution of the escape probability, we get the PL stripes and the transport distance that are consistent with the experiment. We find the cooling speed is the key factor to the transport distance. Based on the comparison between the calculation and the experimental data of transport distance, a function of density, we find increasing the excitation power is not an effective approach to increase the coherent excitons. We also find that the disorders failed to induce the dynamical localization-delocalization transition in the moving lattices. As a result, we infer the sample is basically impurity free.

In order to realize the controllable exciton transport in the moving lattices, according to our studies, two prior-

ity research directions are obvious. Experimental study should still focus on finding the ways of the long lifetime and the fast cooling speed of the excitons. Theoretically, designing achievable moving lattice to realize the dynamical localization-delocalization transition may be a new research direction. After finishing the manuscript, we are aware of the experiment of transport and localization of indirect excitons in a van der Waals MoSe<sub>2</sub>/WSe<sub>2</sub> heterostructure [49]. Whether the theory present in the manuscript can explain the data or not is also worthy of further theoretical study.

## ACKNOWLEDGMENTS

This work was supported by Hebei Provincial Natural Science Foundation of China (Grant No. A2010001116, A2012203174, and D2010001150), and National Natural Science Foundation of China (Grant Nos. 10974169, 11174115 and 10934008).

- 
- [1] Y. Ashida, Z. Gong, and M. Ueda, *Adv. Phys.* **69**, 249 (2021).
- [2] L. Wang, Q. Liu, and Y. Zhang, *Chinese Physics B* **30**, 020506 (2021).
- [3] W.-T. Xue, Y.-M. Hu, F. Song, and Z. Wang, *Phys. Rev. Lett.* **128**, 120401 (2022).
- [4] C. Yuce and H. Ramezani, *Phys. Rev. B* **107**, L140302 (2023).
- [5] L. Xiao, W.-T. Xue, F. Song, Y.-M. Hu, W. Yi, Z. Wang, and P. Xue, “Observation of non-hermitian edge burst in quantum dynamics,” (2023), [arXiv:2303.12831 \[cond-mat.mes-hall\]](https://arxiv.org/abs/2303.12831).
- [6] D. J. Thouless, *Phys. Rev. B* **27**, 6083 (1983).
- [7] L. V. Keldysh and A. N. Kozlov, *Zh. Eksp. Teor. Fiz.* **54** (1968).
- [8] L. V. Butov, C. W. Lai, A. L. Ivanov, A. C. Gossard, and D. S. Chemla, *Nature* **417**, 47 (2002).
- [9] A. G. Winbow, J. R. Leonard, M. Remeika, Y. Y. Kuznetsova, A. A. High, A. T. Hammack, L. V. Butov, J. Wilkes, A. A. Guenther, A. L. Ivanov, M. Hanson, and A. C. Gossard, *Phys. Rev. Lett.* **106**, 196806 (2011).
- [10] C. S. Liu, H. G. Luo, and W. C. Wu, *Journal of Physics: Condensed Matter* **18**, 9659 (2006).
- [11] T. F. Xu, X. L. Jing, H. G. Luo, W. C. Wu, and C. S. Liu, *Journal of Physics: Condensed Matter* **24**, 455301 (2012).
- [12] C. S. Liu, T. F. Xu, Y. H. Liu, and X. L. Jing, *Physica E: Low-dimensional Systems and Nanostructures* **63**, 193 (2014).
- [13] C. S. Liu, H. G. Luo, and W. C. Wu, *Phys. Rev. B* **80**, 125317 (2009).
- [14] R. T. Scalettar, G. G. Batrouni, and G. T. Zimanyi, *Phys. Rev. Lett.* **66**, 3144 (1991).
- [15] P. Lugan, D. Clément, P. Bouyer, A. Aspect, M. Lewenstein, and L. Sanchez-Palencia, *Phys. Rev. Lett.* **98**, 170403 (2007).
- [16] J.-C. Yu, S. Bhave, L. Reeve, B. Song, and U. Schneider, “Observing the two-dimensional bose glass in an optical quasicrystal,” (2023), [arXiv:2303.00737 \[cond-mat.quant-gas\]](https://arxiv.org/abs/2303.00737).
- [17] A. A. High, A. T. Hammack, L. V. Butov, M. Hanson, and A. C. Gossard, *Opt. Lett.* **32**, 2466 (2007).
- [18] L. V. Butov, A. C. Gossard, and D. S. Chemla, *Nature* **418**, 751 (2002).
- [19] D. Snoke, S. Denev, Y. Liu, L. Pfeiffer, and K. West, *Nature* **418**, 754 (2002).
- [20] L. V. Butov, L. S. Levitov, A. V. Mintsev, B. D. Simons, A. C. Gossard, and D. S. Chemla, *Phys. Rev. Lett.* **92**, 117404 (2004).
- [21] R. Rapaport, G. Chen, D. Snoke, S. H. Simon, L. Pfeiffer, K. West, Y. Liu, and S. Denev, *Phys. Rev. Lett.* **92**, 117405 (2004).
- [22] A. V. Balatsky, Y. N. Joglekar, and P. B. Littlewood, *Phys. Rev. Lett.* **93**, 266801 (2004).
- [23] Z. Vörös, D. W. Snoke, L. Pfeiffer, and K. West, *Phys. Rev. Lett.* **97**, 016803 (2006).
- [24] A. A. High, J. R. Leonard, M. Remeika, L. V. Butov, M. Hanson, and A. C. Gossard, *Nano Letters* **12**, 2605 (2012).
- [25] D. Semkat, S. Sobkowiak, G. Manzke, and H. Stolz, *Nano letters* **12**, 5055 (2012).
- [26] L. S. Levitov, B. D. Simons, and L. V. Butov, *Phys. Rev. Lett.* **94**, 176404 (2005).
- [27] A. A. Chernyuk and V. I. Sugakov, *Phys. Rev. B* **74**, 085303 (2006).
- [28] V. I. Sugakov, *Phys. Rev. B* **76**, 115303 (2007).
- [29] C. W. Lai, J. Zoch, A. C. Gossard, and D. S. Chemla, *Science* **303**, 503 (2004).
- [30] P. Bader, S. Blanes, and F. Casas, *The Journal of Chemical Physics* **139**, 124117 (2013).

- [31] A. A. High, A. T. Hammack, L. V. Butov, L. Mouchliadis, A. L. Ivanov, M. Hanson, and A. C. Gossard, *Nano Lett.* **9**, 2094 (2009).
- [32] J. Wilkes, L. Mouchliadis, E. A. Muljarov, A. L. Ivanov, A. T. Hammack, L. V. Butov, and A. C. Gossard, *Journal of Physics: Conference Series* **210**, 012050 (2010).
- [33] J. Y. Zeng, *Quantum Mechanics* (China Science Publishing & Media Ltd, 2007).
- [34] J. J. Sakurai, *Modern Quantum Mechanics* (Addison-Wesley Publishing Company, 1994).
- [35] P. W. Anderson, *Phys. Rev.* **109**, 1492 (1958).
- [36] E. Abrahams, *50 Years of Anderson Localization* (World Scientific, Singapore, 2010).
- [37] X.-G. Zhao, G. A. Georgakis, and Q. Niu, *Phys. Rev. B* **54**, R5235 (1996).
- [38] C.-S. Liu and B.-K. Ma, *Physics Letters A* **315**, 301 (2003).
- [39] X. Cai, L.-J. Lang, S. Chen, and Y. Wang, *Phys. Rev. Lett.* **110**, 176403 (2013).
- [40] X. Q. Sun and C. S. Liu, *Physics Letters A* **482**, 129043 (2023).
- [41] M. Kohmoto, *Phys. Rev. Lett.* **51**, 1198 (1983).
- [42] M. Grifoni and P. Hänggi, *Physics Reports* **304**, 229 (1998).
- [43] C. S. Liu, *Physica E: Low-dimensional Systems and Nanostructures* **134**, 114871 (2021).
- [44] P. G. Harper, *Proceedings of the Physical Society. Section A* **68**, 874 (1955).
- [45] S. Aubry and G. André, *Ann. Isr. Phys. Soc.* **3**, 133 (1980).
- [46] M. Wilkinson and E. J. Austin, *Phys. Rev. B* **50**, 1420 (1994).
- [47] G. S. Jeon, B. J. Kim, S. W. Yi, and M. Y. Choi, *Journal of Physics A: Mathematical and General* **31**, 1353 (1998).
- [48] S. Longhi, *Phys. Rev. B* **103**, 054203 (2021).
- [49] L. H. Fowler-Gerace, Z. Zhou, E. A. Szwed, D. J. Choksy, and L. V. Butov, “Transport and localization of indirect excitons in a van der waals heterostructure,” (2023), arXiv:2307.00702 [cond-mat.mes-hall].